Contents lists available at ScienceDirect

Chemical Engineering Journal

Hierarchical columnar $ZnIn_2S_4/BiVO_4$ Z-scheme heterojunctions with carrier highway boost photocatalytic mineralization of antibiotics

Xingwang Yan [a], Bin Wang [a,b,*], Junze Zhao [a], Gaopeng Liu [a], Mengxia Ji [a], Xiaolin Zhang [b], Paul K. Chu [b], Huaming Li [a], Jiexiang Xia [a,*]

[a] *School of Chemistry and Chemical Engineering, Institute for Energy Research, Jiangsu University, 301 Xuefu Road, Zhenjiang 212013, China*
[b] *Department of Physics, Department of Materials Science and Engineering, and Department of Biomedical Engineering, City University of Hong Kong, Tat Chee Avenue, Kowloon, Hong Kong, China*

ABSTRACT

How to achieve high-speed directional migration and separation of photogenerated carriers at heterointerfaces is still an important factor restricting efficient photocatalytic reactions. Herein, hierarchical columnar $ZnIn_2S_4/BiVO_4$ (ZIS/BVO) Z-scheme composite with photogenerated carriers highway in heterogeneous interface are designed by an *in situ* technique. Ultrathin ZIS nanosheets are uniformly grown upright on the surface of mulberry-like BVO pillars. The confined built-in electric field and Z-scheme heterojunction in ZIS/BVO are verified in detailed by synchronous illumination X-ray photoelectron spectroscopy, theoretical calculation, electron spin resonance spectroscopy, and high-resolution TEM. The photogenerated electrons in the conduction band (CB) of BVO migrate to the valence band (VB) of ZIS through heterojunction, whereas holes in the VB of BVO and electrons in the CB of ZIS maintain the original high redox capability. These holes and electrons with high redox capability react with H_2O and O_2 to generate more $^{\bullet}OH$ and $^{\bullet}O_2^-$, respectively, achieving enhanced photocatalytic mineralization antibiotic properties. The mineralization rate of antibiotics in the optimized ZIS/BVO material are 4.4 and 1.8 times higher than that of pure BVO and ZIS, respectively.

1. Introduction

As a low-cost, efficient, and environmentally friendly technology, semiconductor photocatalysis is one of the effective ways to alleviate the energy crisis and environmental pollution and has attracted wide interests in recent years [1–4]. However, photocatalytic techniques frequently suffer from problems such as the low separation and migration efficiency of photogenerated carriers and weak redox capability [5,6]. Semiconductors with narrow bandgaps can improve utilization of solar energy, but narrowing the bandgap can also lead to serious recombination of photogenerated carriers [7]. In addition, semiconductors with narrow bandgaps show a more negative (positive) position in the VB (CB) and the corresponding oxidation (reducing) ability decreases [8,9]. Consequently, the overall photocatalytic conversion efficiency is unsatisfactory and researchers have been trying to find different ways to improve the separation and migration efficiency of photogenerated carriers as well as the redox capacity of catalysts.

Constructing heterojunctions is an effective approach to improve the separation efficiency of photogenerated charges [10,11]. At present, type-I and type-II heterojunctions can enable directional migration of photogenerated carriers to the bandgap with a small potential energy. However, the redox properties of carriers with low electrical potential are weak and photogenerated carriers with the same electrical charges repel each other, which is not conducive to effective separation of photogenerated carriers [12–15]. In plant photosynthesis, electrons are transported by the Z-scheme transport chains between photosystems I and II [16]. Hence, constructing a Z-scheme heterojunction by imitating plant chloroplasts can inhibit recombination of photogenerated carriers and retain the favorable redox properties of electrons and holes in order to improve the photocatalytic properties.

As a typical ternary metal oxide, $BiVO_4$ (BVO) is widely used in photocatalysis and electrocatalysis due to the excellent physical and chemical properties [17–19]. However, the energy band position of BVO is more positive than that of other semiconducting materials. The holes in the VB of BVO have strong oxidation capability, but the reduction capacity of electrons in the CB of BVO is weak [20,21]. Therefore,

---

* Corresponding authors at: School of Chemistry and Chemical Engineering, Institute for Energy Research, Jiangsu University, 301 Xuefu Road, Zhenjiang 212013, China (B. Wang, J. Xia).
E-mail addresses: wangbin@ujs.edu.cn (B. Wang), xjx@ujs.edu.cn (J. Xia).

choosing the proper semiconductor with a high position of CB is crucial to the design of Z-scheme heterojunctions in BVO. For example, the proper Z-scheme heterojunction can improve the photocatalytic performance of BVO in water splitting [22,23], CO_2 reduction [24,25], and nitrogen fixation [26]. ZIS possesses not only a high-energy band structure, but also excellent optical properties. In addition, preparation of ZIS is simple and the ultrathin ZIS can be attached easily to a semiconductor surface [27–30]. In the ZIS/BVO composites, the surface layered structure is beneficial for light absorption owing to the multiple scattering of light between ZIS nanosheets. Moreover, the flower-like structure on the surface exposes a larger area, which is beneficial for materials to adsorb more reactants including O_2 and pollutants. The construction of ZIS/BVO Z-scheme heterojunctions is beneficial to promote the separation and migration of photogenerated carriers, which can greatly improve the photocatalytic performance of the materials. ZIS/BVO composites are expected to be efficient photocatalysts for water purification. However, although ZIS is a desirable candidate for the Z-scheme heterojunction in BVO, there have been few reports about ZIS/BVO Z-scheme heterojunctions on photocatalysis.

In this work, hierarchical columnar ZIS/BVO composites that produce photogenerated carriers with directional migration properties are designed and fabricated *in situ*. The electron transfer direction is shown to be consistent with that of a Z-scheme system according to synchronous illumination X-ray photoelectron spectroscopy and theoretical calculation. Efficient charge separation and high redox capability can also be accomplished simultaneously and therefore, more active species including $\cdot O_2^-$, h^+, and $\cdot OH$ can be produced to enhance the photocatalytic properties in mineralization of antibiotics. The related mechanism is proposed and discussed.

2. Experimental details

2.1. Materials and synthesis

Bismuth (III) nitrate pentahydrate ($Bi(NO_3)_3 \cdot 5H_2O$), ammonium metavanadate (NH_4VO_3), thioacetamide (TAA), and glycerol were obtained from Sinopharm Chemical Reagent Co., Ltd. Zinc chloride ($ZnCl_2$) and indium chloride tetrahydrate ($InCl_3 \cdot 4H_2O$) were purchased from Shanghai Aladdin Biochemical Technology Co., Ltd. All the chemical reagents were used directly and distilled water was used to prepare the solutions.

2.1.1. Synthesis of mulberry-like BVO

Mulberry-like BVO was synthetized by a hydrothermal method as shown in Fig. 1a. 1 mmol $Bi(NO_3)_3 \cdot 5H_2O$ was dissolved in 15 ml of ethylene glycol to form solution A and 1 mmol NH_4VO_3 was dissolved in 15 ml of distilled water to form solution B. Solution B was added slowly to solution A and stirred for half an hour. The solution was then transferred to a 50 ml Teflon-lined autoclave and heated to 140 °C for 24 h. After the hydrothermal reaction, the product was rinsed several times with distilled water and ethanol and dried at 60 °C for at least 6 h to form the BVO monomer.

2.1.2. Synthesis of flower-like ZIS

The synthetic process is described in Fig. 1b. 20 ml of hydrochloric acid (pH = 2.5) were put in a round bottom flask to which 3 ml of glycerol were added. 0.2 mmol $ZnCl_2$, 0.2 mmol $InCl_3 \cdot 4H_2O$, and 0.4 mmol TAA were added to the solution and stirred for half an hour. The solution was transferred to an oil bath and maintained at 80 °C for 2 h. Afterwards, the products were washed several times with distilled water and ethanol and the ZIS was dried in a vacuum oven at 45 °C for 6 h.

2.1.3. Synthesis of hierarchical columnar ZIS/BVO composites

The synthesis is illustrated in Fig. 1c. A certain amount of BVO (0.05 mmol, 0.10 mmol, 0.15 mmol and 0.20 mmol) was added to a solution of hydrochloric acid (20 ml, pH = 2.5) and glycerol (3 ml). The solution was treated ultrasonically. 0.2 mmol $ZnCl_2$, 0.2 mmol $InCl_3 \cdot 4H_2O$, and 0.4 mmol TAA were added to the solution in turn and the following steps were as same as those for ZIS. The corresponding samples were labeled as ZIS/BVO-0.05, ZIS/BVO-0.10, ZIS/BVO-0.15, and ZIS/BVO-0.20, respectively.

2.2. Characterization

Scanning electron microscopy (SEM, JOEL JSM-7800F), transmission electron microscopy (TEM, Fei talos 200×) and high-resolution transmission electron microscopy (HR-TEM, Fei talos 200×) were used to examine the morphology of the catalysts. X-ray diffraction (XRD) was carried out on the Shimadzu XRD-6000X-ray diffractometer with Cu K_α irradiation. The FT-IR spectra were acquired by diffuse reflectance infrared Fourier transform spectroscopy (Nicolet iS50, Thermo Electron Corporation) and UV–vis diffuse reflectance spectra (UV–vis DRS) were obtained on the UV-3600 Plus spectrophotometer (Shimadzu Corporation, Japan). Synchronous illumination X-ray photoelectron spectroscopy (SI-XPS, Thermo ESCALAB 250Xi) was performed to determine the elemental composition and chemical states of the samples. The intermediates in TC degradation were analyzed by liquid chromatography-mass spectrometry (LC-MS) (Thermo, *thermo LXQ LC/MS) in which the mobile phase contained 30 % methanol and 70 % water and the flow rate was 1.0 µL/min. The specific surface area and
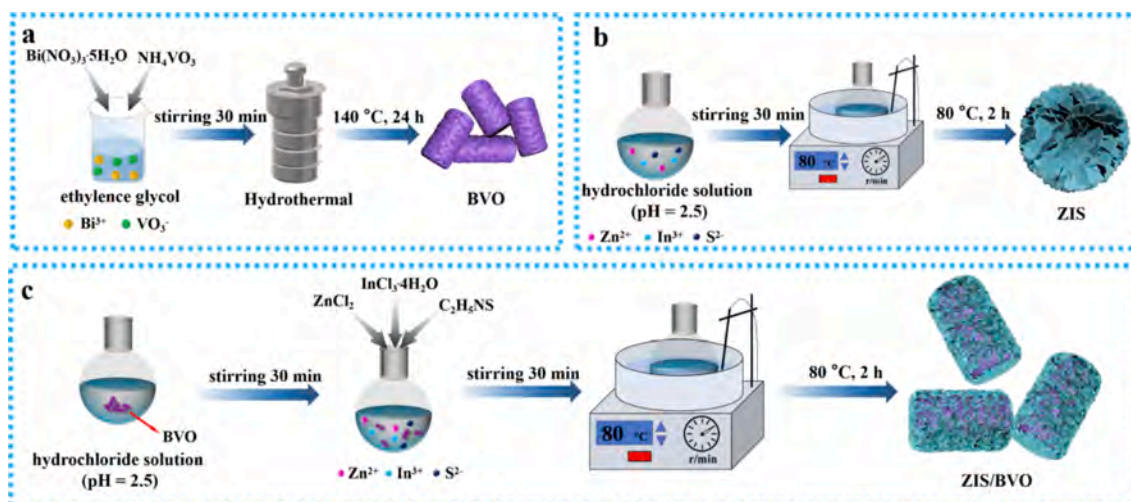

Fig. 1. Schematic illustration of the synthesis of (a) BVO, (b) ZIS, and (c) ZIS/BVO composites.

particle size were determined based on the N_2 adsorption–desorption isotherms using the surface area analyzer (Micromeritics Instrument Corporation, USA). Electrochemical impedance spectroscopy (EIS) was conducted in a solution of 0.1 M KCl and 5 mM $Fe(CN)_6^{3-}/Fe(CN)_6^{4-}$ and the electrochemical signals were recorded on the CHI 760E electrochemical analyzer (Chenhua Instrument Company).

2.3. DFT calculation

The Vienna Abinitio Simulation Package (VASP) was used to perform the density functional theory (DFT) calculations via the projected augmented wave method (PAW) [31]. The Perdew-Burke-Ernzerhof (PBE) functional was adopted to treat the exchange–correlation energy within the generalized gradient approximation (GGA) [32]. BVO, ZIS and ZIS/BVO-0.10 structures were optimized firstly. The energy cutoff for the plane wave was 420 eV and the k-point was $3 \times 3 \times 1$. The convergence criterion for structural optimization and energy were set to 0.03 eV/Å and 10^{-4} eV, respectively. Then, k-point was set to be $9 \times 9 \times 1$ and the destiny of state (DOS) calculations of three structures were further carried out [33].

2.4. Photocatalytic experiments

50 mg of the samples were dispersed in 100 ml of the TC solution (20 mg L^{-1}) and a system with circulating water was employed to ensure that the temperature was constant at 30 °C in order to reduce the effects of thermal catalysis. An air pump was used to provide ample oxygen in the reaction. A Pyrex photocatalytic reactor was equipped with a 250 W Xe lamp (Wavelength: 420 nm, Operating Voltage: 220 V, Yangzhou University Town Science and Education Equipment Co., ltd.). Prior to light irradiation, the suspensions were stirred for 30 min to establish the adsorption and desorption equilibrium between the sample and target pollutant in darkness. The Xe lamp was turned on for the light reaction. About 4 ml of the suspension were collected every 0.5 h and the particles in the suspensions were removed by centrifugation. The absorbance of the solution was monitored by UV–vis spectrophotometry at 356 nm and the photocatalytic characteristics were derived according to the absorbance.

3. Results and discussion

3.1. Structure and morphology characterization of catalysts

SEM is performed to observe the morphology of the samples. As shown in Fig. 2a, the BVO monomer resembles a mulberry with a rough surface and diameter and length of about 1.5 μm and 3 μm, respectively. Fig. S1a depicts the morphology of pure ZIS which shows flower-like spheres with a diameter of 1 μm assembled from some ultra-thin nanosheets. The SEM images of ZIS/BVO-0.10 are shown in Fig. 2b, c. The mulberry-like BVO is evenly decorated with ZIS nanosheets and no agglomeration is observed. When the amount of BVO is decreased, the ZIS monomer shows obvious agglomeration in ZIS/BVO-0.05 (Fig. S1b). However, when the content of BVO in the composites is increased, the ZIS nanosheets do not completely wrap BVO in ZIS/BVO-0.15 (Fig. S1c) and ZIS/BVO-0.20 (Fig. S1d) and the large amount of exposed BVO reduces utilization of the materials. TEM and HR-TEM are performed to examine the morphology and microstructure of the samples as shown in Fig. 2d-f. ZIS is evenly distributed on the surface of BVO which has a flimsy sheet-like structure as shown in Fig. 2d, e. The ZIS nanosheets form tight contact with BVO. The HR-TEM images of ZIS/BVO-0.10 in Fig. 2f reveal interplanar spacings of 0.310 nm and 0.205 nm corresponding to the (−1 2 1) crystal facets of BVO and (5 1 1) crystal facets of ZIS, respectively. The crystal facets of BVO and ZIS are interlaced confirming formation of the heterojunction between ZIS and BVO [34]. The TEM-EDS maps of ZIS/BVO-0.10 in Fig. 2g reveal the presence of six elements: Bi, V, O, Zn, In, and S in the ZIS/BVO composites. Bi, V, and O are distributed in the middle BVO and Zn, In, and S are detected from the outer ZIS constituting a hierarchical columnar structure.

The specific surface areas of BVO, ZIS, and ZIS/BVO-0.10 are determined from the nitrogen adsorption–desorption isotherms (Fig. S2) to be 2.6963, 31.6915, and 27.4534 m^2/g, respectively. Compared to BVO, the specific surface areas of the composites increase due to the
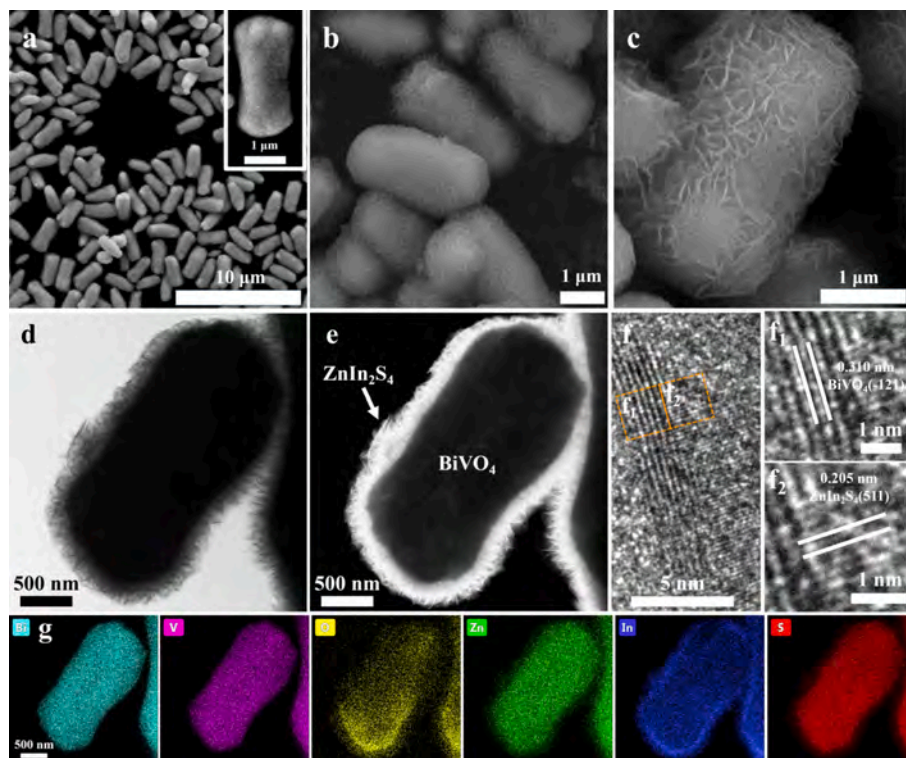

Fig. 2. SEM images of (a) BVO and (b, c) ZIS/BVO-0.10, (d, e) TEM image, (f) HR-TEM image, and (g) Elemental maps of ZIS/BVO-0.10.

sheet-like structure of ZIS. The large specific surface area enables exposure of more active sites to boost the photocatalytic activity.

XRD is utilized to analyze the structure of the materials. The XRD pattern of BVO can be indexed to the monoclinic phase BVO (JCPDS NO. 14-0688) as shown in Fig. 3a. The main diffraction peaks at 18.9°, 28.9°, 30.5°, and 39.8° belong to the (0 1 1), (1 2 1), (0 4 0) and (2 1 1) crystal facets of BVO, respectively [35]. The XRD pattern of ZIS matches the hexagonal phase of ZIS (JCPDS NO. 65-2023). The results confirm that the BVO and ZIS monomer have high purity. The XRD peaks from the ZIS/BVO composites are similar to those from the BVO monomer and no characteristic peaks of ZIS appear from the ZIS/BVO composites. The possible explanation is that the peak intensity of ZIS is too weak. However, with decreasing BVO content, the peak intensity increases slightly. There is a strong interaction between ZIS and BVO. The FT-IR spectra of BVO, ZIS, and ZIS/BVO-0.10 in Fig. 3b reveal two strong vibrational bands at 711 cm^{-1} and 815 cm^{-1} from BVO stemming from waging and symmetrical stretching of V-O [36], respectively. With regard to the single ZIS, the distinct absorption peak at 1613 cm^{-1} is assigned to the bending mode of H—O—H of residual water molecules adsorbed on the ZIS surface [37]. The characteristic peaks observed from both BVO and ZIS corroborate formation of the ZIS/BVO heterojunction.

The optical absorption capacity is studied by UV–vis DRS. Fig. 3c shows that the light absorption band edges of BVO and ZIS are about 539 nm and 487 nm, respectively. Obviously, all the ZIS/BVO absorption edges show red-shifts and the visible light response range of BVO broadens [38]. The bandgaps (E$_g$) of ZIS and BVO monomer can be computed by the following equation: $\alpha h\nu = A (h\nu - E_g)^{n/2}$. The $(\alpha E_{photon})^{1/2}$ vs E$_{photon}$ curve of the two monomers is determined by the classic Tauc approach and the E$_g$ values of ZIS and BVO are 2.39 and 2.17 eV, respectively (Fig. 3d). According to a previous report [39], the VB values of BVO and ZIS are 0.28 and −0.96 eV, respectively and the CB values of BVO and ZIS are determined to be 2.45 and 1.43 eV based on $E_{CB} = E_{VB} - E_g$. The density of states (DOS) is calculated to study the band composition and hybridization states [40] as shown in Fig. 3e, f. The valence band maximum (VBM) of ZIS is mainly made up of the S 2p orbitals, whereas the conduction band minimum (CBM) of ZIS mainly consists of the In 3d and S 2p orbitals. The VBM of BVO is made up of the O 2p orbits including partial hybridization with the 6p orbitals of Bi and 5d orbitals of V. Meanwhile, the CBM of BVO comprises mainly the V 5d orbital with some hybridization with the 6p orbital of Bi and 2p orbital of O [41].

3.2. Research on Z-scheme mechanism of ZnIn$_2$S$_4$/BiVO$_4$ material

The electron localization function (ELF) is used to analyze the electron distribution and transfer between atoms [42]. Fig. 4a-d show the electron distribution in the materials. When ZIS is in contact with BVO, the electron cloud of BVO changes significantly as shown in Fig. 4d. As shown in Fig. 4e, the blue and red shaded areas represent exhaustion and accumulation of the electron density, respectively. When there is close contact between ZIS and BVO, the atoms in BVO appear in red implying that electrons in ZIS are transferred to BVO. The work functions (Φ) of ZIS, BVO, and ZIS/BVO-0.10 are calculated by the following formula: $\Phi = E_{vac} - E_F$, where E$_{vac}$ is the electrostatic potential in vacuum and E$_F$ is the Fermi level [43,44]. The work functions of the ZIS, BVO and ZIS/BVO-0.10 surfaces are 6.67, 5.87, and 6.12 eV, respectively (Fig. 4f-h). Obviously, the Fermi level of the BVO surface is lower than that of ZIS and that of ZIS/BVO-0.10 is between ZIS and BVO. When the ZIS and BVO form close contact, electrons in ZIS are transferred to BVO to balance the Fermi level of the composite [45] and an internal electric field is created at the interface between ZIS and BVO.

Theoretical calculation is performed to study the changes of the electronic structure in the ground state and that of the composites in the photo-excited state is investigated by SI-XPS. The XPS survey spectra of ZIS, BVO, and ZIS/BVO-0.10 are displayed in Fig. S3a. Only six elements (Bi, V, O, Zn, In and S) are observed from ZIS/BVO-0.10 confirming the high purity. The two peaks at 159.09 eV and 164.38 eV are attributed to Bi 4f$_{7/2}$ and Bi 4f$_{5/2}$ (Fig. 5a). Similarly, the O 1s spectrum exhibits two peaks at 529.80 and 531.75 eV corresponding to lattice oxygen and adsorbed oxygen, respectively (Fig. S3c). The peak shape of O 1s of ZIS/BVO-0.10 is irregular because of the effects of ZIS surface-adsorbed oxygen. The characteristic peaks of V 2p are not found from the composites (Fig. S3b) probably because of the large amount of ZIS covering the BVO surface. The peaks of Zn 2p at 1,022.1 and 1,045.0 eV of ZIS are Zn 2p$_{3/2}$ and Zn 2p$_{1/2}$ (Fig. 5b). The fitted peaks of In 3d at 444.8 and 452.3 eV in Fig. 5c arise from In 3d$_{5/2}$ and In 3d$_{3/2}$, respectively. As shown in Fig. 5d, the S 2p peaks at 161.90 and 162.99 eV belong to S 2p$_{3/2}$ and S 2p$_{1/2}$, respectively. When the ZIS/BVO heterojunction is formed, the Bi 4f and O 1s orbitals of ZIS/BVO-0.10 shift negatively compared to the BVO monomer, suggesting accumulation of electrons in the BVO. In contrast, the Zn 2p, In 3d, and S 2p orbitals of ZIS/BVO-0.10 shift positively compared to pure ZIS, indicating loss of electrons from ZIS. The XPS results demonstrate that electrons are transferred from ZIS to BVO after forming a close contact between ZIS and BVO. In this case,
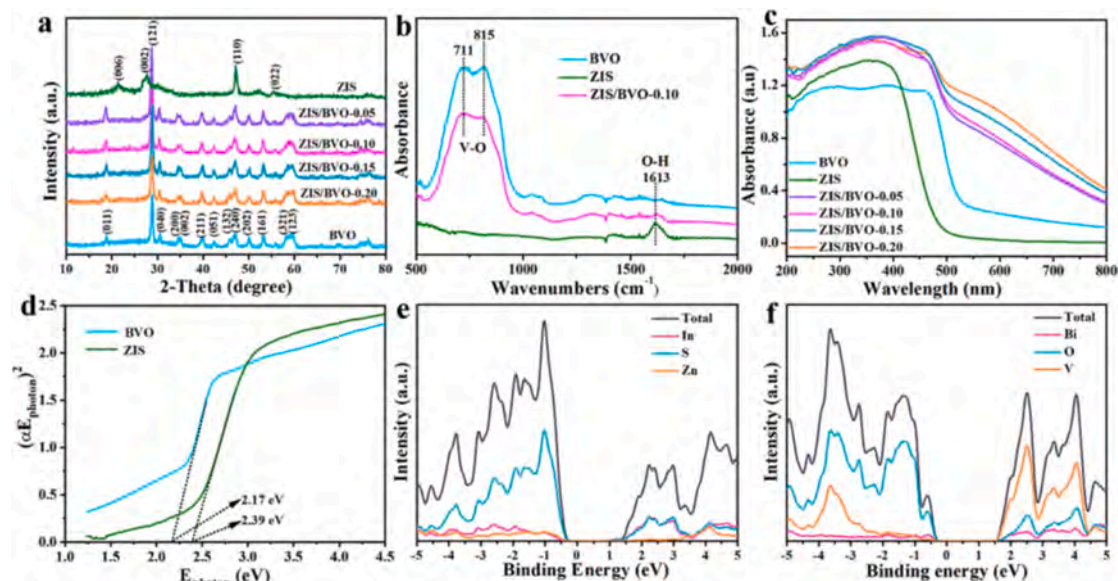

Fig. 3. (a) XRD patterns, (b) FT-IR spectra, and (c) UV–vis DRS of the samples, (d) Bandgaps of BVO and ZIS, and calculated DOS of (e) ZIS and (f) BVO.
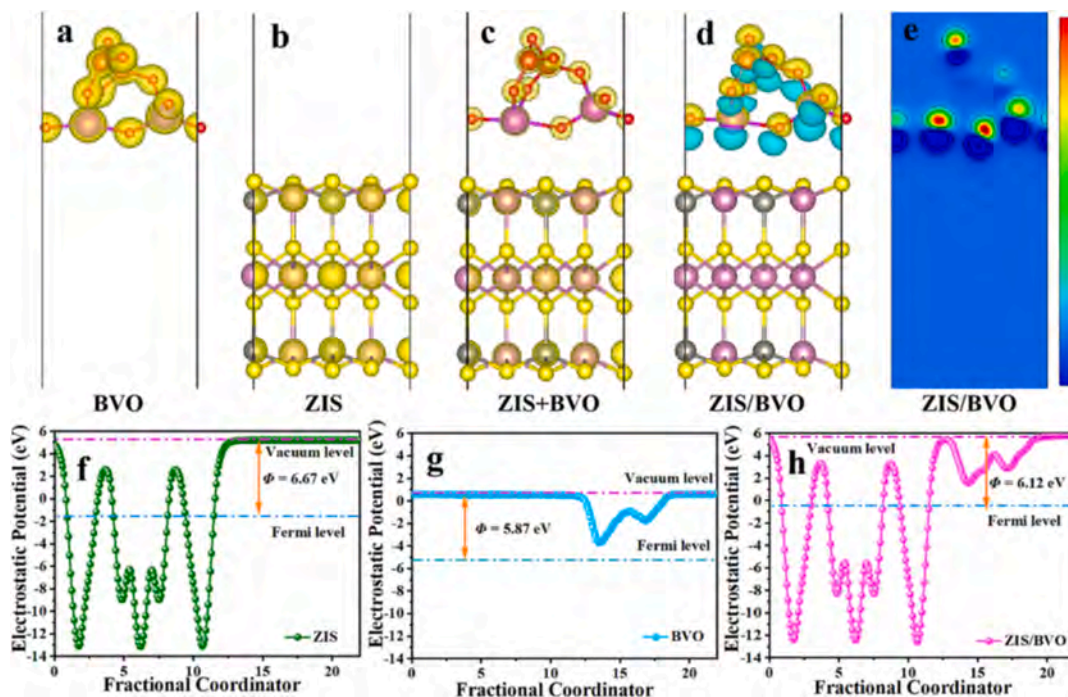
Fig. 4. Electron distributions of (a) BVO, (b) ZIS, (c) ZIS + BVO, and (d) ZIS/BVO, (e) ELF of ZIS/BVO, and calculated work functions of (f) ZIS, (g) BVO, and (h) ZIS/BVO.
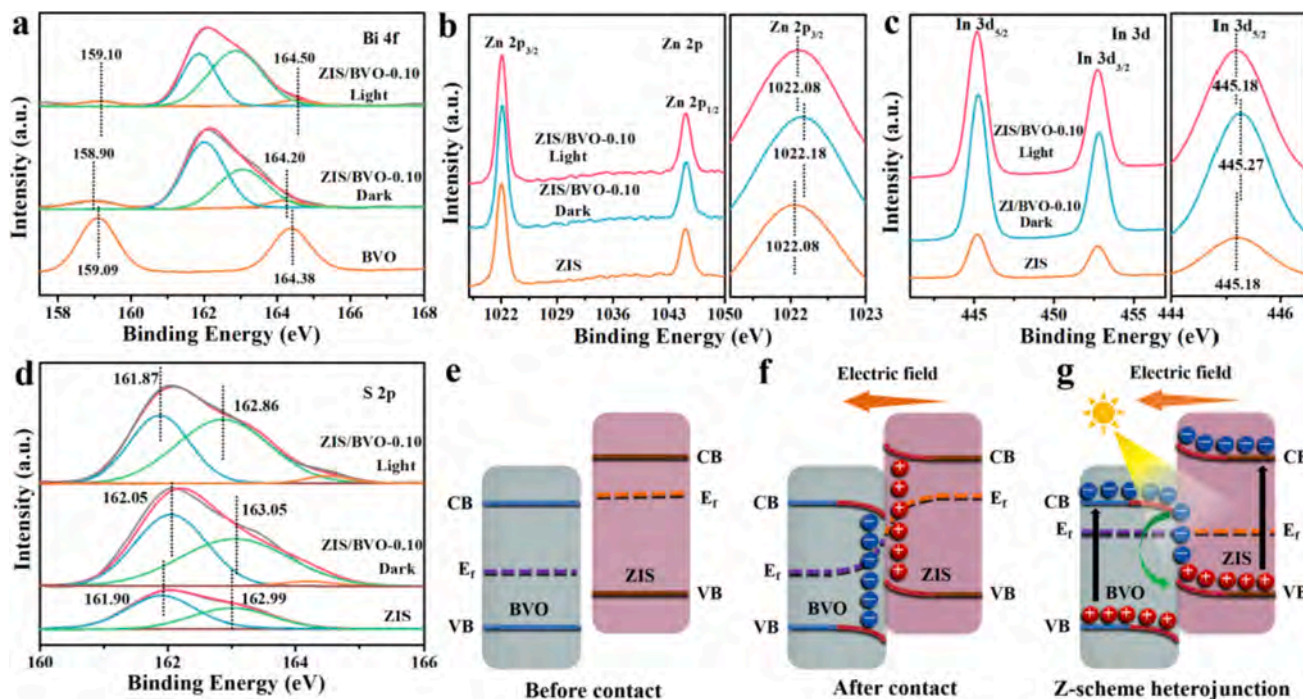

Fig. 5. XPS spectra of (a) Bi 4*f*, (b) Zn 2*p*, (c) In 3*d*, and (d) S 2*p* and flow direction of charges (e) before contact, (f) after contact, and (g) under light irradiation.

ZIS can be considered as a reductive photocatalyst with a higher Fermi level and BVO can be considered an oxidative photocatalyst with a lower Fermi level (Fig. 5e) [46]. Thermodynamically, electrons transfer from ZIS to BVO until the Fermi level is tantamount (Fig. 5f). The interfaces of ZIS and BVO possess positive and negative charges, respectively and therefore, an internal electrical field is established between ZIS and BVO with a direction from ZIS to BVO. When the ZIS/BVO-0.10 heterojunction is excited upon light irradiation, the Bi 4*f* and O 1*s* orbitals shift positively compared to those in the dark. In contrast, the Zn 2*p*, In 3*d*,

and S 2*p* orbitals of ZIS/BVO-0.10 show negative shifts under light irradiation, suggesting that photogenerated electrons are transferred from BVO to ZIS in the photoexcited state. With regard to ZIS and BVO, the photogenerated electrons are excited to CB during light irradiation. The excited electrons in the CB of BVO combine with holes in the VB of ZIS through the built-in electric field at the heterojunction interface (Fig. 5g). The direction of electrical transfer after contact and upon irradiation is consistent with the Z-scheme mechanism and XPS shows that the above analysis of electron localization and work functions is

reasonable.

3.3. Enhancement of photocatalytic TC degradation activity

Antibiotics with strong inhibitory effects on pathogenic bacteria are widely used in the treatment of human diseases. However, wastewater containing large amounts of antibiotics is sometimes discharged directly into rivers and residual antibiotics are difficult to break down in the natural environment consequently causing serious water pollution. Therefore, it is necessary to degrade residual antibiotics in the environment. Among them, TC is a typical broad-spectrum antibiotic. Because of its low price, TC has become the main antibiotic in the world. Due to its stable structure and resistance to biodegradation, it has been frequently detected in surface waters in recent years [47]. Traditional methods such as adsorption and membrane separation cannot completely decompose it. In addition, chemical or biological methods may cause secondary pollution [48]. Photocatalytic method is an ideal approach to water purification. Therefore, TC was selected for degradation experiments. As shown in Fig. 6a, TC is hardly degraded without a photocatalyst and so self-degradation of TC is insignificant. The photocatalytic activity of BVO monomer is not ideal and only about 26 % of TC is removed after visible light exposure for 3 h. ZIS also shows a low degradation efficiency by degrading only 45 % of TC after 3 h. In comparison, all the ZIS/BVO composites show significantly better degradation characteristics than ZIS and BVO monomer. Among the composites, ZIS/BVO-0.10 delivers the best photocatalytic degradation performance. About 60 % of TC can be removed in the presence of ZIS/BVO-0.10 after light irradiation for 3 h. The kinetics of photocatalytic degradation of TC shows the following relationship of $-\ln (C/C_0) = kt$ (k is the kinetic rate constant) (Fig. 6b). The kinetic rate constants of ZIS, BVO, ZIS/BVO-0.05, ZIS/BVO-0.10, ZIS/BVO-0.15, and ZIS/BVO-0.20

are 0.00375, 0.00155, 0.00453, 0.00682, 0.00441, and 0.00443 min^{-1}, respectively. Therefore, the kinetic rate constants of all the ZIS/BVO composites are larger than those of ZIS and BVO and specifically, the kinetic rate constants of ZIS/BVO-0.10 with the best degradation efficiency are about 2 times and 4.5 times as high as those of ZIS and BVO, respectively. For comparison, ZnO, TiO₂, BiOBr and C₃N₄ are chosen to perform photocatalytic degradation experiments under the same conditions. As shown in Fig. S4a, the efficiency of them to degrade TC are 48 %, 40 %, 26 % and 2 % after 3 h light irradiation, respectively. However, ZIS/BVO-0.10 can degrade 60 % of TC after 3 h light irradiation. The kinetic rate constants of the ZIS/BVO-0.10 are larger than that of the other four photocatalysts from the reaction kinetic curves (Fig. S4b). It is suggested that the photocatalytic degradation performance of ZIS-BVO materials is higher than that of these photocatalysts.

Mineralization of organic pollutants by ZIS/BVO-0.10 is assessed by TOC analysis during degradation (Fig. S7a) [49]. The TOC removal efficiency of ZIS/BVO-0.10 is higher than that of ZIS and BVO and ZIS/BVO-0.10 fares better in TC mineralization consistent with the results of degradation. In order to investigate the degradation process of TC, the intermediates formed during photocatalytic degradation are monitored by LC-MS and the possible degradation pathway is derived. Fig. S5 shows the mass spectra of the solution at different time revealing formation of many small molecules during degradation. According to the detected intermediates, the degradation path of TC is proposed. As shown in Fig. 6c, TC ($m/z = 445$) with electron-rich functional groups are attacked by $^\bullet O_2^-$ and $^\bullet OH$ to form intermediate $P1$ ($m/z = 362$) by demethylation, additional reaction, and elimination of the amide group. $P1$ is further converted into intermediate $P2$ ($m/z = 302$) through dehydroxylation and ring-opening reaction. After further attack by $^\bullet O_2^-$ and $^\bullet OH$, $P3$ ($m/z = 244.3$) is produced by breaking carbon–carbon single bond. Afterwards, $P3$ is converted into $P4$ ($m/z = 186$) by ring
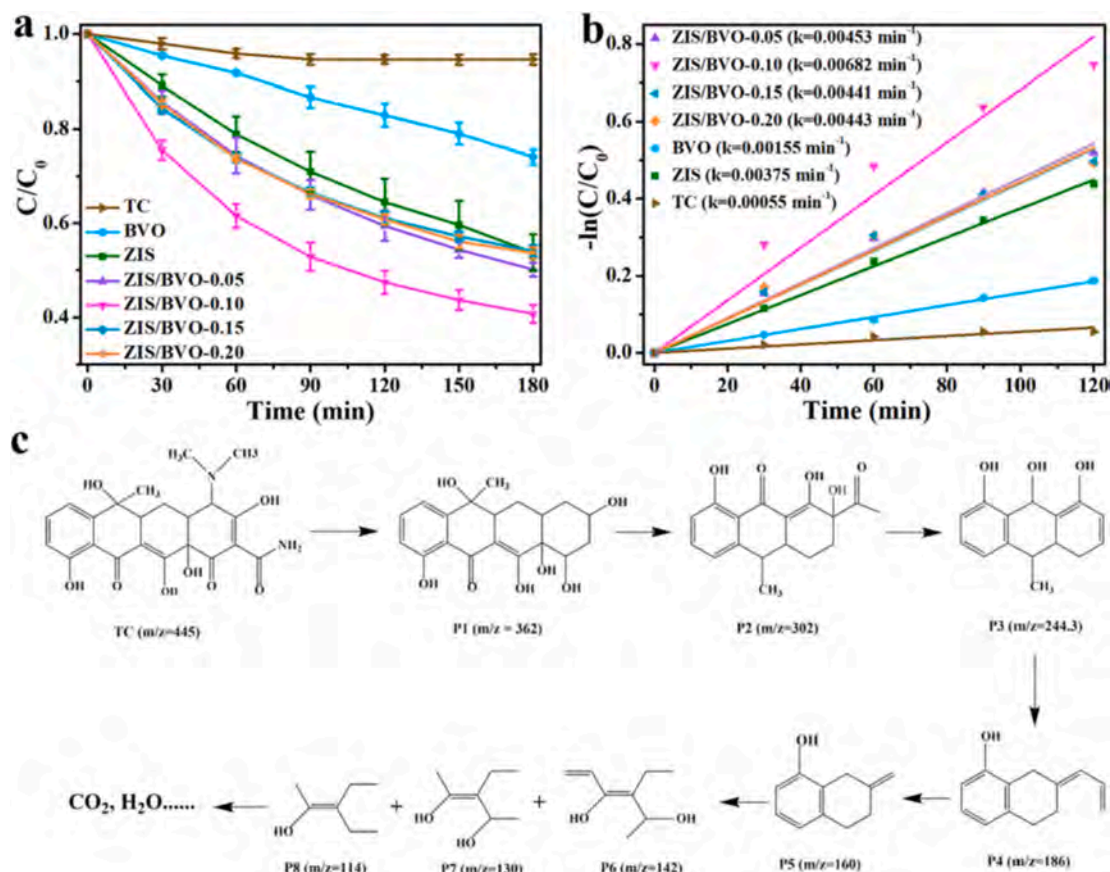

Fig. 6. Photocatalytic properties of the samples for degradation of TC under visible light irradiation, (b) Reaction kinetics for degradation of TC, and (c) Possible degradation pathways of TC in ZIS/BVO-0.10.

opening, dihydroxylation, and demethylation. P5 ($m/z = 160$) is formed by breaking the carbon–carbon single bond and after a series of ring opening, P5 ($m/z = 160$) is decomposed to form *P*6 ($m/z = 142$), P7 ($m/z = 130$), and P8 ($m/z = 144$). Finally, these small molecules are gradually mineralized into CO_2 and H_2O.

This work further explores the effects of anions and pH value in solution on the photocatalytic degradation reaction. 0.1 mmol of NaCl, $NaNO_3$, Na_2SO_4 and Na_2CO_3 were added to the pollutants to study the effect of anions on the photocatalytic reaction. As is shown in Fig. S6a, the photocatalytic degradation performance of ZIS/BVO-0.10 materials is not significantly reduced after adding these anions, which indicates that the presence of anions has no effect on the photocatalytic degradation process. The anti-interfere experiments prove that ZIS/BVO materials possess good anti-ion interference performance. In addition, the pH value of the solution was adjusted to the target value using 2 mol/L NaOH and HNO3. Then the photocatalytic degradation experiment was carried out. As shown in the Fig. S6b, the degradation

efficiency of TC is almost unchanged under alkaline conditions. However, the degradation of TC was significantly inhibited under acidic conditions. The possible reason is that the adsorption performance of photocatalysts to pollutants decreases under acidic conditions, resulting in a decrease in the overall degradation efficiency.

The stability of ZIS/BVO-0.10 is evaluated by cycling experiments. As shown in Fig. S7b, the photocatalytic degradation properties of ZIS/BVO-0.10 worsen after cycling for 9 times. The photocatalysts after cycling are collected to perform XRD (Fig. S7c) and SEM (Fig. S7d) and as shown, the structure and morphology of ZIS/BVO-0.10 do not change significantly. Furthermore, ZIS/BVO-0.10 composites after photocatalysis reactions were collected for XPS characterization. It can be seen from Fig. S8 that Bi, V, O, Zn, In and S elements are still detected in the used ZIS/BVO-0.10 composites. Fig.S9 displays the high resolution XPS spectra of fresh samples and used sample. Compared with the fresh samples, the positions of each element for the used sample have no obvious shift. The results of XPS indicate the stable structure of ZIS/BVO
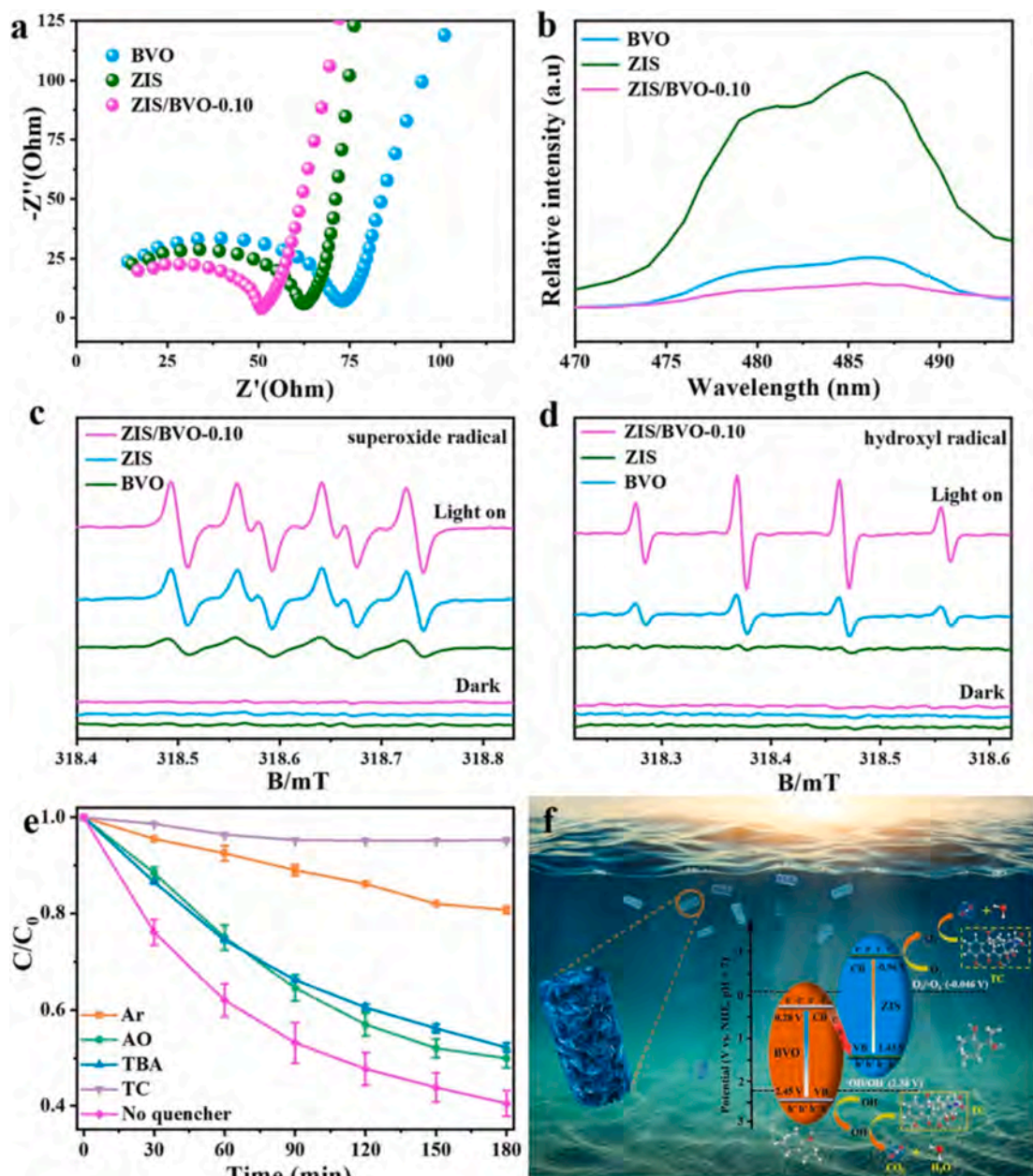

Fig. 7. (a) EIS spectra, (b) PL spectra, and ESR spectra of (c) DMPO-•O_2^- and (d) DMPO-•OH of ZIS, BVO and ZIS/BVO-0.10; (e) Photocatalytic degradation of TC in the presence of different radical scavengers; (d) Mechanism of ZIS/BVO-0.10 in photocatalytic degradation.

composites.

3.4. Optical, electronic and mechanistic studies of catalysts

To investigate the resistance of the materials during charge transfer, EIS is carried out (Fig. 7a). The resistance is gauged by the Nyquist plot diameter and a smaller diameter implies a smaller resistance [50]. It is clear that the Nyquist diameter of the composites is smaller than those of ZIS and BVO and the resistance of ZIS/BVO-0.10 is smaller thus favoring charge transport. The steady-state PL spectra are acquired to analyze separation and recombination of photoexcited electrons and holes in the photocatalysts. As expected, fluorescence from ZIS/BVO-0.10 is weaker than that from ZIS and BVO (Fig. 7b), indicating that recombination of photogenerated charges is inhibited and so the Z-scheme heterojunction improves separation and migration efficiency of photogenerated carriers.

ESR and free radicals capturing experiments are performed to determine the active species in the degradation process [51,52]. The ESR results are presented in Fig. 7c, d. Without light, no signals are observed for DMPO-$\cdot O_2^-$ and DMPO-$\cdot OH$ from the three materials and no reactive oxygen species are produced under dark conditions. However, upon light illumination, all three materials produce signal peaks of DMPO-$\cdot O_2^-$ and the signal from ZIS/BVO-0.10 is significantly stronger than those from ZIS and BVO. Furthermore, DMPO-$\cdot OH$ is observed from BVO and ZIS/BVO-0.10 with the signal from the latter being stronger indicating that more $\cdot O_2^-$ and $\cdot OH$ are generated at ZIS/BVO-0.10. However, DMPO-$\cdot OH$ cannot be observed from ZIS because the VB position of ZIS is more negative than that of $\cdot OH/OH^-$ (2.38 V vs NHE) and holes in the VB of ZIS cannot convert OH^- into $\cdot OH$. This verifies that electrons in the CB of BVO combine with holes in the VB of ZIS when ZIS/BVO-0.10 is excited by visible light. The holes in the VB of BVO can oxidize H_2O to generate $\cdot OH$ and meanwhile, electrons in the CB of ZIS have reducing power to convert O_2 into more $\cdot O_2^-$. To further verify the presence of these reactive oxygen species, free radical trapping experiments are performed in the presence of ZIS/BVO-0.10 (Fig. 7e). Argon (Ar), *tert*-butyl alcohol (TBA), and ammonium oxalate (AO) are the $\cdot O_2^-$, $\cdot OH$, and h^+ capturing agents, respectively [53]. After Ar is introduced to the reaction, the degradation efficiency of TC is greatly reduced. This indicates that a large amount of $\cdot O_2^-$ is produced and $\cdot O_2^-$ plays an important role in the degradation process. In addition, notable inhibition of photocatalytic degradation is observed after adding AO and TBA further validating that $\cdot O_2^-$, holes, and $\cdot OH$ are the main active species. The results from the radical capture experiments are in line with ESR revealing that photogenerated carriers are transferred *via* the Z-scheme mechanism in the photoexcited state.

The reaction mechanism of the ZIS/BVO-0.10 Z-scheme heterojunction is proposed according to the positional relationship of VB and CB and active species. As shown in Fig. 7f, electrons in the VB of ZIS and BVO are excited and then transferred to the CB. Because of the internal electric field between ZIS and BVO, electrons in the CB of BVO recombine with holes in the VB of ZIS, while electrons in the VB of ZIS and holes in the CB of BVO are retained. Owing to more negative position of the CB of ZIS, electrons in ZIS reduce O_2 to $\cdot O_2^-$ ($E^0(O_2/\cdot O_2^-) = -0.046$ eV vs NHE). The VB position of BVO is more positive than that of $E^0(\cdot OH/OH^-)$ (2.38 eV vs NHE). Holes in the BVO thus not only convert OH^- into $\cdot OH$, but also directly oxidize organic pollutants. Eventually, $\cdot O_2^-$, $\cdot OH$ and h^+ convert the organic pollutants into CO_2 and H_2O. In summary, the ZIS/BVO-0.10 Z-scheme heterojunction not only separates photogenerated electrons and holes, but also retains the maximum redox capacity of the original materials.

This work is the first to synthesize mulberry-like BVO by a simple hydrothermal method under neutral conditions and grow ultrathin ZIS nanosheets on its surface. ZIS/BVO composites exhibit good photocatalytic performance of degrading TC. However, the only disadvantage is that the specific surface area of the composites is not improved compared to ZIS monomer. If the specific surface areas of composites are increased by different methods, this material will exhibit better photocatalytic performance and this material will also be more used to solve wastewater.

4. Conclusion

A hierarchical columnar ZIS/BVO Z-scheme heterojunction is designed and fabricated. Flower-like ZIS nanosheets are prepared uniformly on the surface of mulberry-like BVO. Synchronous illumination X-ray photoelectron spectroscopy and theoretical calculation confirm that the photoexcited electrons are transferred from BVO to ZIS *via* the Z-scheme mechanism. This strategy not only accomplishes effective separation of photogenerated carriers, but also maintain robust oxidation and reduction centers in the materials. Compared to pure BVO and ZIS, ZIS/BVO has better photocatalytic properties in mineralization of antibiotics. In the degradation process, $\cdot O_2^-$, $\cdot OH$, and h^+ are the main active species. The reaction mechanism is proposed and discussed. The concept of constructing a Z-scheme heterojunction between two semiconductors with the suitable band positions is promising in improving the activity and efficiency of photocatalysts.

CRediT authorship contribution statement

Xingwang Yan: Conceptualization, Data curation, Investigation, Writing – original draft. **Bin Wang:** Conceptualization, Resources, Writing – review & editing, Supervision. **Junze Zhao:** Data curation, Investigation, Writing – original draft. **Gaopeng Liu:** Data curation, Investigation. **Mengxia Ji:** Resources, Supervision. **Xiaolin Zhang:** Data curation, Investigation. **Paul K. Chu:** Resources, Writing – review & editing, Supervision. **Huaming Li:** Resources, Writing – review & editing, Supervision. **Jiexiang Xia:** Conceptualization, Resources, Writing – review & editing, Supervision.

Declaration of Competing Interest

The authors declare that they have no known competing financial interests or personal relationships that could have appeared to influence the work reported in this paper.

Data availability

Data will be made available on request.

Acknowledgements

Appendix A. Supplementary data

Supplementary data to this article can be found online at https://doi.org/10.1016/j.cej.2022.139271.

References

[1] Q. Wang, K. Domen, Particulate photocatalysts for light-driven water splitting: Mechanisms, challenges, and design strategies, Chem. Rev. 120 (2020) 919–985, https://doi.org/10.1021/acs.chemrev.9b00201.

[2] X. Li, C. Garlisi, Q. Guan, S. Anwer, K. Al-Ali, G. Palmisano, L. Zheng, A review of material aspects in developing direct Z-scheme photocatalysts, Mater. Today 47 (2021) 75–107, https://doi.org/10.1016/j.mattod.2021.02.017.

[3] Q. Guo, C. Zhou, Z. Ma, X. Yang, Fundamentals of TiO₂ photocatalysis: Concepts, mechanisms, and challenges, Adv. Mater. 31 (2019) 1901997, https://doi.org/10.1002/adma.201901997.

[4] S. Sun, L. He, M. Yang, J. Cui, S. Liang, Facet junction engineering for photocatalysis: A comprehensive review on elementary knowledge, facet-synergistic mechanisms, functional modifications, and future perspectives, Adv. Funct. Mater. 32 (2022) 2106982, https://doi.org/10.1002/adfm.202106982.

[5] H. Zhu, X. Yuan, Q. Yao, J. Xie, Shining photocatalysis by gold-based nanomaterials, Nano Energy 88 (2021) 106306, https://doi.org/10.1016/j.nanoen.2021.106306.

[6] L. Zhang, J. Zhang, H. Yu, J. Yu, Emerging S-scheme photocatalyst, Adv. Mater. 34 (2022) 2107668, https://doi.org/10.1002/adma.202107668.

[7] B. Dai, Y. Yu, Y. Chen, H. Huang, C. Lu, J. Kou, Y. Zhao, Z. Xu, Construction of self-healing internal electric field for sustainably enhanced photocatalysis, Adv. Funct. Mater. 29 (2019) 1807934, https://doi.org/10.1002/adfm.201807934.

[8] Q. Liang, X. Liu, G. Zeng, Z. Liu, L. Tang, B. Shao, Z. Zeng, W. Zhang, Y. Liu, M. Cheng, W. Tang, S. Gong, Surfactant-assisted synthesis of photocatalysts: Mechanism, synthesis, recent advances and environmental application, Chem. Eng. J. 372 (2019) 429–451, https://doi.org/10.1016/j.cej.2019.04.168.

[9] Q. Liang, S. Ploychompoo, J. Chen, T. Zhou, H. Luo, Simultaneous Cr(VI) reduction and bisphenol a degradation by a 3D Z-scheme Bi₂S₃-BiVO₄ graphene aerogel under visible light, Chem. Eng. J. 384 (2020) 123256, https://doi.org/10.1016/j.cej.2019.123256.

[10] B.J. Ng, L.K. Putri, X.Y. Kong, Y.W. Teh, P. Pasbakhsh, S.P. Chai, Z-scheme photocatalytic systems for solar water splitting, Adv. Sci. 7 (2020) 1903171, https://doi.org/10.1002/advs.201903171.

[11] S. Chen, J.J.M. Vequizo, Z. Pan, T. Hisatomi, M. Nakabayashi, L. Lin, Z. Wang, K. Kato, A. Yamakata, N. Shibata, T. Takata, T. Yamada, K. Domen, Surface modifications of (ZnSe)₀.₅(CuGa₂.₅Se₄.₂₅)₀.₅ to promote photocatalytic Z-scheme overall water splitting, J. Am. Chem. Soc. 143 (2021) 10633–10641, https://doi.org/10.1021/jacs.1c03555.

[12] V. Hasija, V.H. Nguyen, A. Kumar, P. Raizada, V. Krishnan, A.A.P. Khan, P. Singh, E. Lichtfouse, C. Wang, P. Huong, Advanced activation of persulfate by polymeric g-C₃N₄ based photocatalysts for environmental remediation: A review, J. Hazard. Mater. 413 (2021) 125324, https://doi.org/10.1016/j.jhazmat.2021. 125324.

[13] H. Cai, B. Wang, L. Xiong, J. Bi, L. Yuan, G. Yang, S. Yang, Orienting the charge transfer path of type-II heterojunction for photocatalytic hydrogen evolution, Appl. Catal. B 256 (2019) 117853, https://doi.org/10.1016/j.apcatb. 2019.117853.

[14] C. Rocks, V. Svrcek, T. Velusamy, M. Macias-Montero, P. Maguire, D. Mariotti, Type-I alignment in MAPbI₃ based solar devices with doped-silicon nanocrystals, Nano Energy 50 (2018) 245–255, https://doi.org/10.1016/j.nanoen.2018.05.036.

[15] W. Qian, S. Xu, X. Zhang, C. Li, W. Yang, C.R. Bowen, Y. Yang, Diferences and similarities of photocatalysis and electrocatalysis in two-dimensional nanomaterials: Strategies, traps, applications and challenges, Nano-Micro Lett. 13 (2021) 156, https://doi.org/10.1007/s40820-021-00681-9.

[16] J. Cai, X. Liu, Z. Gao, L. Li, H. Wang, Chlorophylls derivatives: Photophysical properties, assemblies, nanostructures and biomedical applications, Mater. Today 45 (2021) 77–92, https://doi.org/10.1016/j.mattod.2020.11.001.

[17] M. Tayebi, B.K. Lee, Recent advances in BiVO₄ semiconductor materials for hydrogen production using photoelectrochemical water splitting, Renewable Sustainable Energy Rev. 111 (2019) 332–343, https://doi.org/10.1016/j.rser.2019. 05.030.

[18] R. Gao, S. Liu, X. Guo, R. Zhang, J. He, X. Liu, T. Nakajima, X. Zhang, L. Wang, Pt-induced defects curing on BiVO₄ photoanodes for near-threshold charge separation, Adv. Energy Mater. 11 (2021) 2102384, https://doi.org/10. 1002/aenm.202102384.

[19] H. Wu, R. Irani, K. Zhang, L. Jing, H. Dai, H.Y. Chung, F.F. Abdi, Y.H. Ng, Unveiling carrier dynamics in periodic porous BiVO₄ photocatalyst for enhanced solar water splitting, ACS Energy Lett. 6 (2021) 3400-3407, https://doi.org/10. 1021/acsenergylett.1c01454.

[20] Z. Long, Q. Li, T. Wei, G. Zhang, Z. Ren, Historical development and prospects of photocatalysts for pollutant removal in water, J. Hazard. Mater. 395 (2020) 122599, https://doi.org/10.1016/j.jhazmat.2020.122599.

[21] L. Buzzetti, G.E.M. Crisenza, P. Melchiorre, Mechanistic studies in photocatalysis, Angew. Chem. Int. Ed. 58 (2019) 3730-3747, https://doi.org/10. 1002/anie.201809984.

[22] K. Ye, H. Li, D. Huang, S. Xiao, W. Qiu, M. Li, Y. Hu, W. Mai, H. Ji, S. Yang, Enhancing photoelectrochemical water splitting by combining work function tuning and heterojunction engineering, Nat. Commun. 10 (2019) 3687, https://doi.org/10.1038/s41467-019-11586-y.

[23] D. Dai, X. Liang, B. Zhang, Y. Wang, Q. Wu, X. Bao, Z. Wang, Z. Zheng, H. Cheng, Y. Dai, B. Huang, P. Wang, Strain adjustment realizes the photocatalytic overall water splitting on tetragonal zircon BiVO₄, Adv. Sci. 9 (2022) 2105299, https://doi.org/10.1002/advs.202105299.

[24] R. Das, S. Sarkar, R. Kumar, S.D. Ramarao, A. Cherevotan, M. Jasil, C.P. Vinod, A. K. Singh, S.C. Peter, Noble-metal-free heterojunction photocatalyst for selective CO₂ reduction to methane under induced strain relaxation, ACS Catal. 12 (2022) 687–697, https://doi.org/10.1021/acscatal.1c04587.

[25] M. Lu, Q. Li, C. Zhang, X. Fan, L. Li, Y. Dong, G. Chen, H. Shi, Remarkable photocatalytic activity enhancement of CO₂ conversion over 2D/2D g-C₃N₄/BiVO₄ Z-scheme heterojunction promoted by efficient interfacial charge transfer, Carbon 160 (2020) 342–352, https://doi.org/10.1016/j.carbon.2020. 01.038.

[26] Y. Liu, P. Deng, R. Wu, R.A. Geioushy, Y. Li, Y. Liu, F. Zhou, H. Li, C. Sun, BiVO₄/TiO₂ heterojunction with rich oxygen vacancies for enhanced electrocatalytic nitrogen reduction reaction, Front. Phys. 16 (2021) 53503, https://doi.org/10.1007/s11467-021-1067-8.

[27] Y. Wang, M. Liu, C. Wang, C. Wu, J. Gao, M. Li, Z. Xing, Z. Li, W. Zhou, Hollow nanoboxes Cu₂₋ₓS@ZnIn₂S₄ core-shell S-scheme heterojunction with broad-spectrum response and enhanced photothermal-photocatalytic performance, Small 18 (2022) 2202544, https://doi.org/10.1002/smll.202202544.

[28] Y. He, C. Chen, Y. Liu, Y. Yang, C. Li, Z. Shi, Y. Han, S. Feng, Quantitative evaluation of carrier dynamics in full-spectrum responsive metallic ZnIn₂S₄ with indium vacancies for boosting photocatalytic CO₂ reduction, Nano Lett. 22 (2022) 4970–4978, https://doi.org/10.1021/acs.nanolett.2c01666.

[29] G. Han, X. Liu, Z. Cao, Y. Sun, Photocatalytic pinacol C-C coupling and jet fuel precursor production on ZnIn₂S₄ nanosheets, ACS Catal. 10 (2020) 9346–9355, https://doi.org/10.1021/acscatal.0c01715.

[30] P. Jin, L. Wang, X. Ma, R. Lian, J. Huang, H. She, M. Zhang, Q. Wang, Construction of hierarchical ZnIn₂S₄@PCN-224 heterojunction for boosting photocatalytic performance in hydrogen production and degradation of tetracycline hydrochloride, Appl. Catal. B 284 (2021) 119762, https://doi.org/10.1016/j.apcatb.2020.119762.

[31] B. Wang, W. Zhang, G. Liu, H. Chen, Y. Weng, H. Li, P. Chu, J. Xia, Excited Electron-Rich Bi⁽³⁻ˣ⁾⁺ Sites: A Quantum Well-Like Structure for Highly-Promoted Selective Photocatalytic CO₂ Reduction Performance, Adv. Funct. Mater. 32 (2022) 2202885, https://doi.org/10.1002/adfm.202202885.

[32] L. Luo, L. Fu, H. Liu, Y. Xu, J. Xing, C. Chang, D. Yang, J. Tang, Synergy of Pd atoms and oxygen vacancies on In₂O₃ for methane conversion under visible light, Nat. Commun. 13 (2022) 2930, https://doi.org/101038/s41467-022- 30434-0.

[33] J. Zhao, M. Ji, H. Chen, Y. Weng, J. Zhong, Y. Li, S. Wang, Z. Chen, J. Xia, H. Li, Interfacial chemical bond modulated Bi₁₉S₂₇Br₃/g-C₃N₄ Z-scheme heterojunction for enhanced photocatalytic CO₂ conversion, Appl. Catal. B 307 (2022) 121162, https://doi.org/10.1016/j.apcatb.2022.121162.

[34] B. Wang, S. Yang, H. Chen, Q. Gao, Y. Weng, W. Zhu, G. Liu, Y. Zhang, Y. Ye, H. Zhu, H. Li, J. Xia, Revealing the role of oxygen vacancies in bimetallic PbBiO₂Br atomic layers for boosting photocatalytic CO₂ conversion, Appl. Catal. B 277 (2020) 119170, https://doi.org/10.1016/j.apcatb.2020.119170.

[35] B. Baral, K. Parida, {040/110} Facet isotype heterojunctions with monoclinic scheelite BiVO₄, Inorg. Chem. 59 (2020) 10328-10342, https://dx.doi.org/10. 1021/acs.inorgchem.0c01465.

[36] S. Chen, D. Huang, G. Zeng, W. Xue, L. Lei, P. Xu, R. Deng, J. Li, M. Cheng, In-situ synthesis of facet-dependent BiVO₄/Ag₃PO₄/PANI photocatalyst with enhanced visible-light-induced photocatalytic degradation performance: Synergism of interfacial coupling and hole-transfer, Chem. Eng. J. 382 (2020) 122840, https://doi.org/10.1016/j.cej.2019.122840.

[37] J. Fu, B. Chang, Y. Tian, F. Xi, X. Dong, Novel C₃N₄-CdS composite photocatalysts with organic-inorganic heterojunctions: in suit synthesis, exceptional activity, high stability and photocatalytic mechanism, J. Mater. Chem. A 1 (2013) 3083–3090, https://doi.org/10.1039/C2TA00672C.

[38] L.K. Ng, E.J. Tan, T.W. Goh, X. Zhao, Z. Chen, T.C. Sum, H.S. Soo, Mesoporous SiO₂/BiVO₄/CuOₓ nanospheres for Z-scheme, visible light aerobic C-N coupling and dehydrogenation, Appl Mater Today 15 (2019) 192–202, https://doi.org/10.1016/j.apmt.2019.01.010.

[39] J. Hu, C. Chen, Y. Zheng, G. Zhang, C. Guo, C. Li, Spatially separating redox centers on Z-scheme ZnIn₂S₄/BiVO₄ hierarchical heterostructure for highly efficient photocatalytic hydrogen evolution, Small 16 (2020) 2002988, https://doi.org/10.1002/smll.202002988.

[40] T. Hussain, M. Sajjad, D. Singh, H. Bae, H. Lee, J.A. Larsson, R. Ahuja, A. Karton, Sensing of volatile organic compounds on two-dimensional nitrogenated holey graphene, graphdiyne, and their heterostructure, Carbon 163 (2020) 213–223, https://doi.org/10.1016/j.carbon.2020.02.078.

[41] J. Safaei, H. Ullah, N.A. Mohamed, M.F.M. Noh, M.F. Soh, A.A. Tahir, N.A. Ludin, M.A. Ibrahim, W.N.R.W. Isahak, M.A.M. Teridi, Enhanced photoelectrochemical performance of Z-scheme g-C₃N₄/BiVO₄ photocatalyst, Appl. Catal. B 234 (2018) 296–310, https://doi.org/10.1016/j.apcatb.2018.04.056.

[42] V. Pasumarthi, T. Liu, M. Dupuis, Charge carrier transport dynamics in W/Mo-doped BiVO₄: first principles-based mesoscale characterization, J. Mater. Chem. A 7 (2019) 3054–3065, https://doi.org/10.1039/c8ta09899a.

[43] Z. Han, Y. Zhao, G. Gao, W. Zhang, Y. Qu, H. Zhu, P. Zhu, G. Wang, Erbium single atom composite photocatalysts for reduction of CO₂ under visible light: CO₂ molecular activation and 4f levels as an electron transport bridge, Small 17 (2021) 2102089, https://doi.org/10.1002/smll.202102089.

[44] Y. Lin, C. Yang, Q. Niu, S. Luo, Interfacial charge transfer between silver phosphate and W₂N₃ induced by nitrogen vacancies enhances removal of β-Lactam antibiotics, Adv. Funct. Mater. 32 (2021) 2108814, https://doi.org/10. 1002/adfm.202108814.

[45] B. Wang, J. Zhao, H. Chen, Y. Weng, H. Tang, Z. Chen, W. Zhu, Y. She, J. Xia, H. Li, Unique Z-scheme carbonized polymer dots/Bi₄O₅Br₂ hybrids for efficiently boosting photocatalytic CO₂ reduction, Appl. Catal. B 293 (2021) 120182, https://doi.org/10.1016/j.apcatb.2021.120182.

[46] Q. Xu, L. Zhang, B. Cheng, J. Fan, J. Yu, S-scheme heterojunction photocatalyst, Chem 6 (2020) 1543–1559, https://doi.org/10.1016/j.chempr.2020.06.010.

[47] Y. Zhang, J. Zhou, X. Chen, L. Wang, W. Cai, Coupling of heterogeneous advanced oxidation processes and photocatalysis in efficient degradation of tetracycline hydrochloride by Fe-based MOFs: Synergistic effect and degradation pathway, Chem. Eng. J. 369 (2019) 745–757, https://doi.org/10.1016/j.cej.2019.03.108.

[48] Q. Chen, H. Zhou, J. Wang, J. Bi, F. Dong, Activating earth-abundant insulator BaSO₄ for visible-light induced degradation of tetracycline, Appl. Catal. B 307 (2022) 121182, https://doi.org/10.1016/j.apcatb.2022.121182.

[49] L. Tang, J. Wang, C. Jia, G. Lv, G. Xu, W. Li, L. Wang, J. Zhang, M. Wu, Simulated solar driven catalytic degradation of psychiatric drug carbamazepine with binary

BiVO$_4$ heterostructures sensitized by graphene quantum dots, Appl. Catal. B 205 (2017) 587–596, https://doi.org/10.1016/j.apcatb.2016.10.067.

[50] Q. Su, L. Zhu, M. Zhang, Y. Li, S. Liu, J. Lin, F. Song, W. Zhang, S. Zhu, j. Pan, Construction of a bioinspired hierarchical BiVO$_4$/BiOCl heterojunction and its enhanced photocatalytic activity for phenol degradation, ACS Appl. Mater. Interfaces 13 (2021) 32906–32915, https://doi.org/10.1021/acsami.1c05117.

[51] C. Zhang, S. Tian, F. Qin, Y. Yu, D. Huang, A. Duan, C. Zhou, Y. Yang, W. Wang, Y. Zhou, Catalyst-free activation of permanganate under visible light irradiation for

sulfamethazine degradation: Experiments and theoretical calculation, Water Res. 194 (2021) 116915, https://doi.org/10.1016/j.watres.2021.116915.

[52] Y. Li, H. Dong, L. Li, J. Xiao, Efficient degradation of sulfamethazine via activation of percarbonate by chalcopyrite, Water Res. 202 (2021) 117451, https://doi.org/10.1016/j.watres.2021.117451.

[53] M.X. Ji, Y.F. Shao, E. Nkudede, Z.H. Liu, X. Sun, J.Z. Zhao, Z.R. Chen, S. Yin, H. M. Li, J.X. Xia, Oxygen vacancy triggering the broad-spectrum photocatalysis of bismuth oxyhalide solid solution for ciprofloxacin removal, J. Colloid Interf. Sci. 626 (2022) 221–230, https://doi.org/10.1016/j.jcis.2022.06.076.

Supporting Materials

Hierarchical columnar ZnIn$_2$S$_4$/BiVO$_4$ Z-scheme heterojunctions with carrier highway boost photocatalytic mineralization of antibiotics

Xingwang Yan[a], Bin Wang[a,b,*], Junze Zhao[a], Gaopeng Liu[a], Mengxia Ji[a], Xiaolin Zhang[b], Paul K. Chu[b], Huaming Li[a], Jiexiang Xia[a,*]

[a] *School of Chemistry and Chemical Engineering, Institute for Energy Research, Jiangsu University, 301 Xuefu Road, Zhenjiang 212013, China*

[b] *Department of Physics, Department of Materials Science and Engineering, and Department of Biomedical Engineering, City University of Hong Kong, Tat Chee Avenue, Kowloon, Hong Kong, China*

E-mail: wangbin@ujs.edu.cn (B. Wang); xjx@ujs.edu.cn (J. X. Xia)
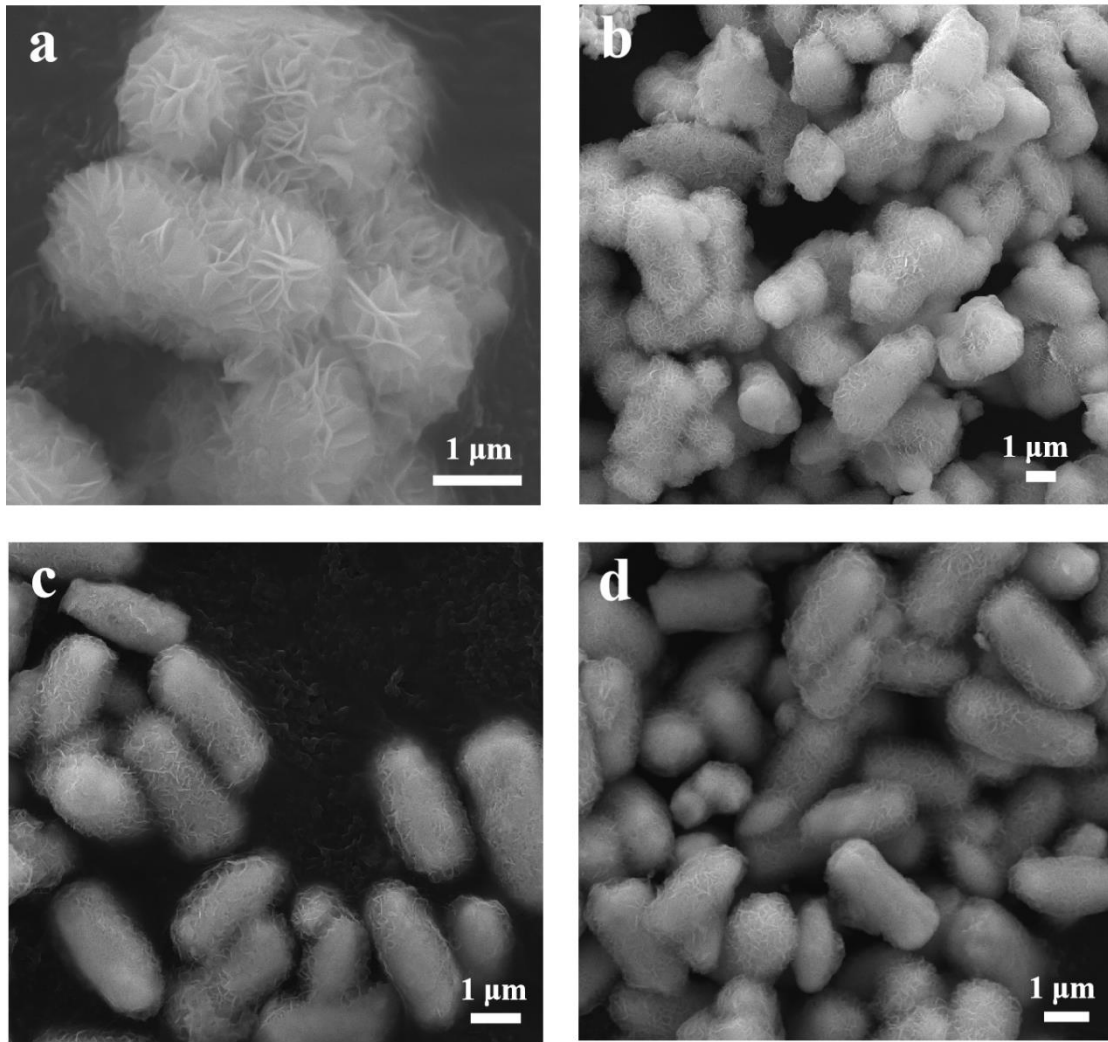
Fig. S1. SEM images of (a) ZIS nanoflowers, (b) ZIS/BVO-0.05, (c) ZIS/BVO-0.15, and (d) ZIS/BVO-0.20 composites.
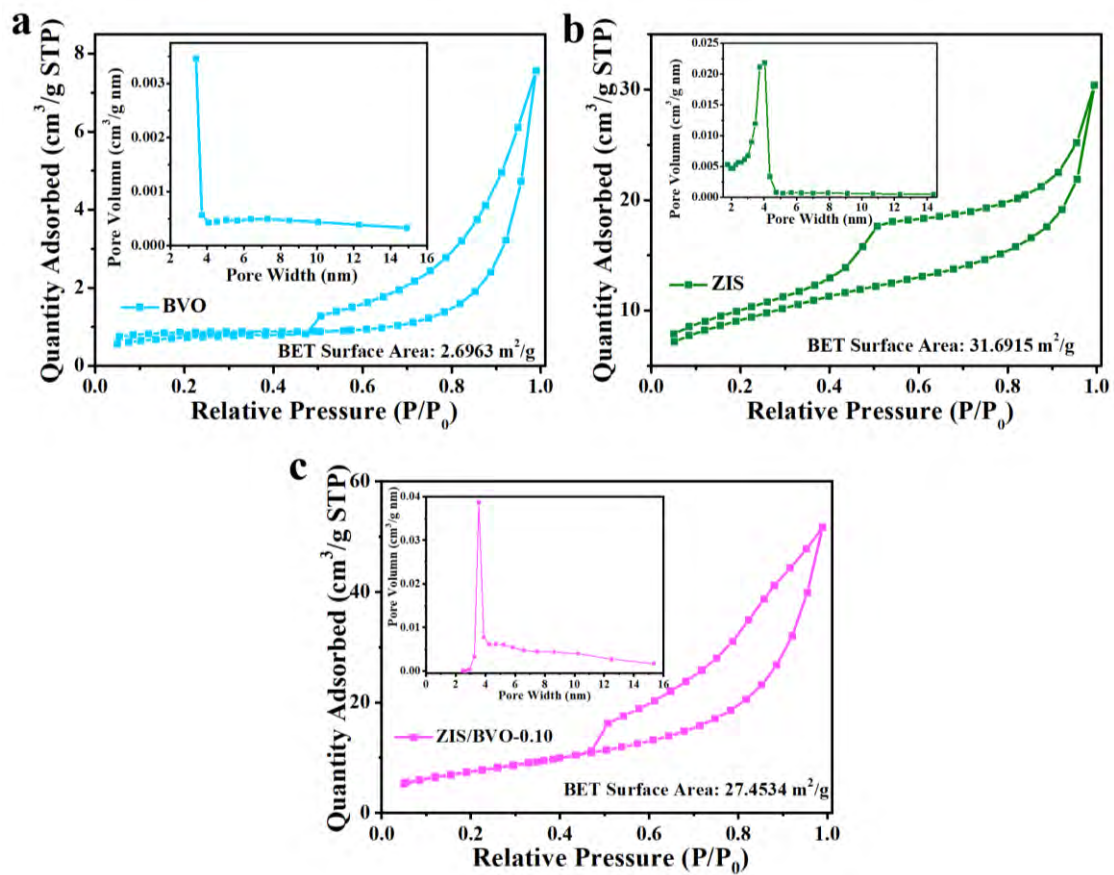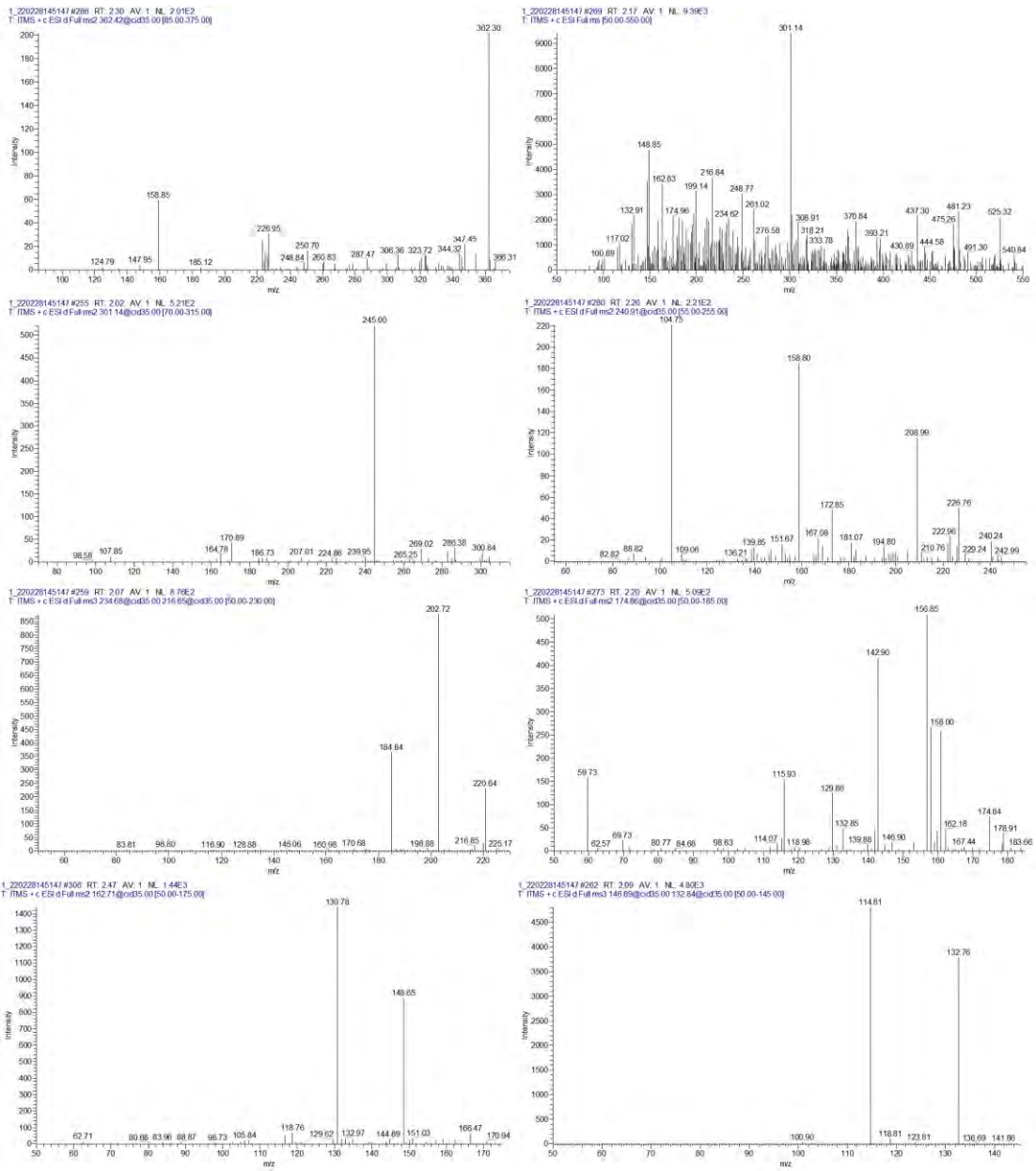
Fig. S2. Nitrogen absorption-desorption isotherms of (a) BVO, (b) ZIS, and (c) ZIS/BVO-0.10 composites.
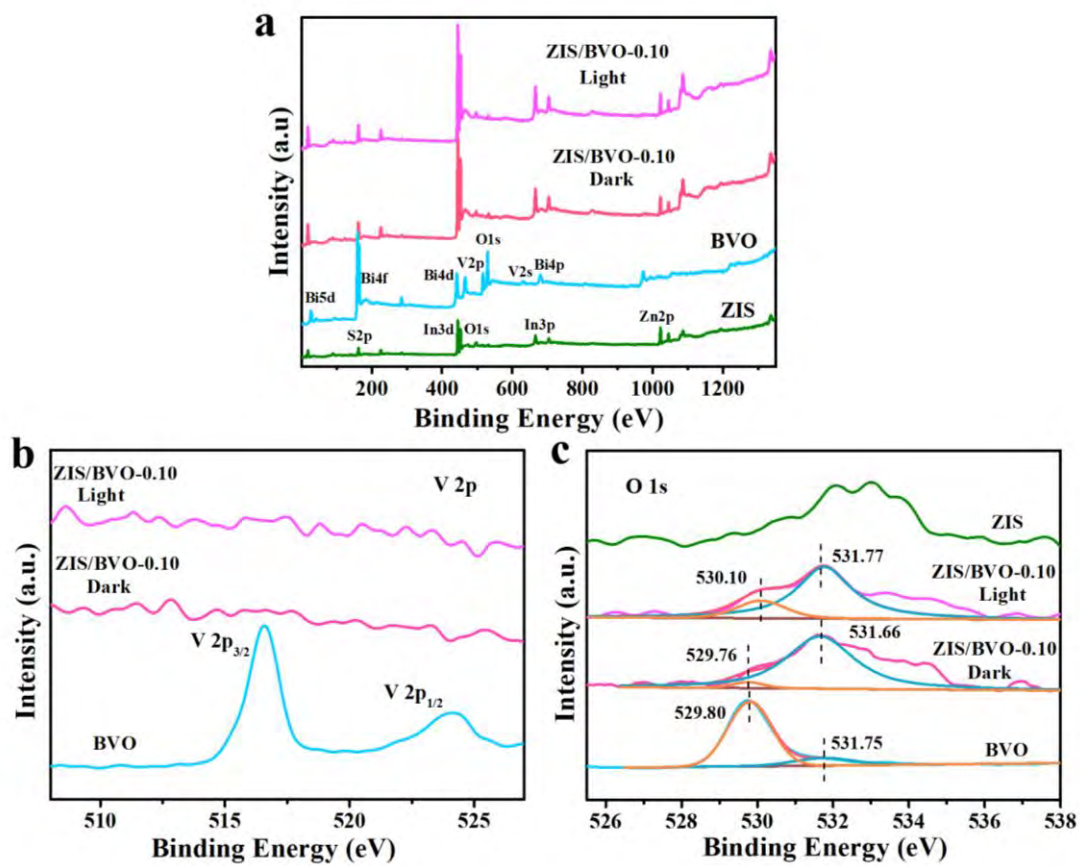
Fig. S3. (a) XPS survey spectra of ZIS, BVO, and ZIS/BVO-0.10 and high-resolution

XPS spectra of (b) V $2p$ and (c) O $1s$.
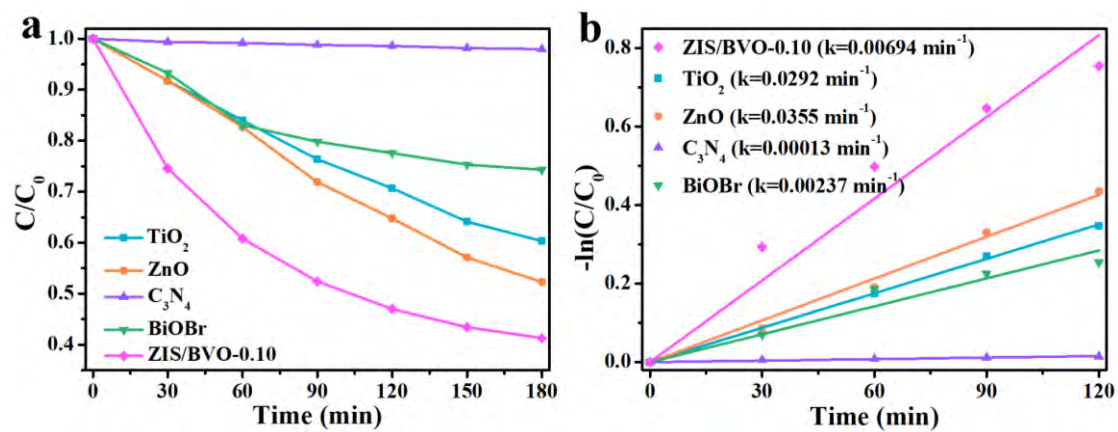
Fig. S4. (a) Photocatalytic properties and (b) reaction kinetics of different photocatalysts for degradation of TC under visible light irradiation.

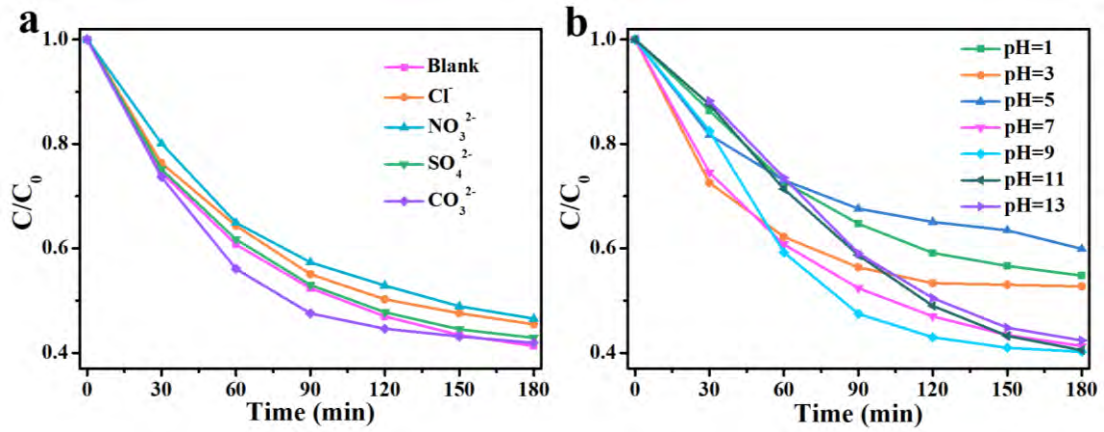**Fig. S5.** LC-MS spectra of TC and intermediates in the photodegradation process

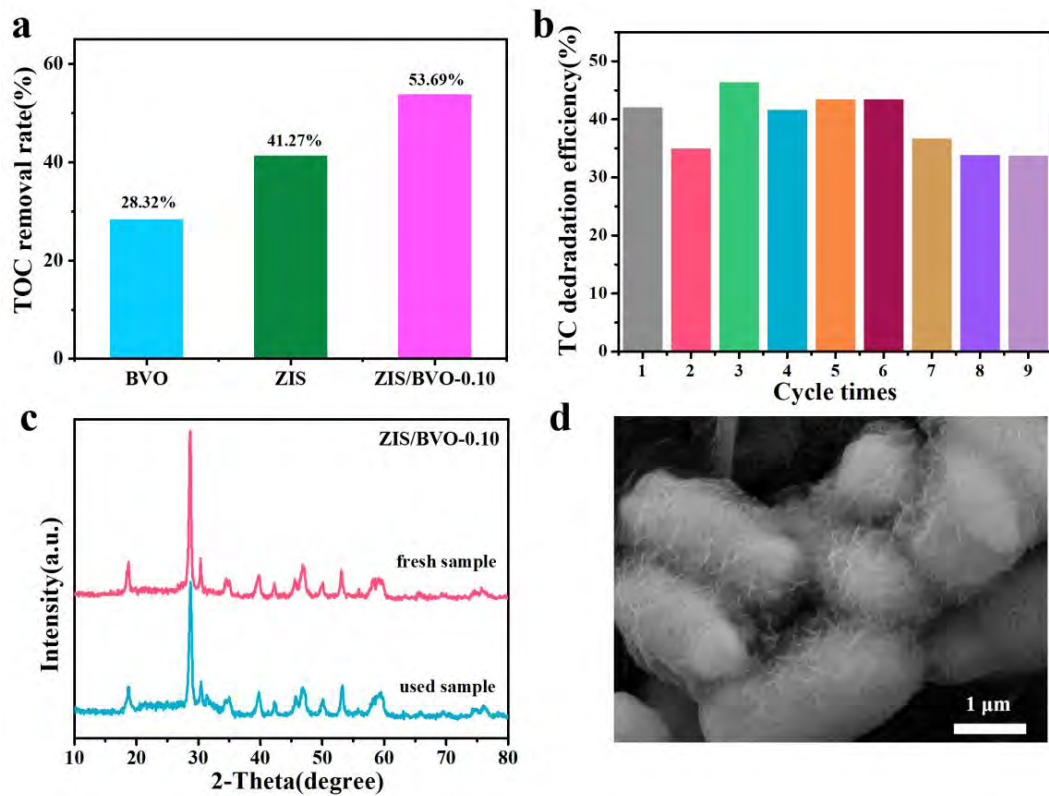**Fig. S6.** Effects of (a) anions and (b) pH values on the degradation of TC.
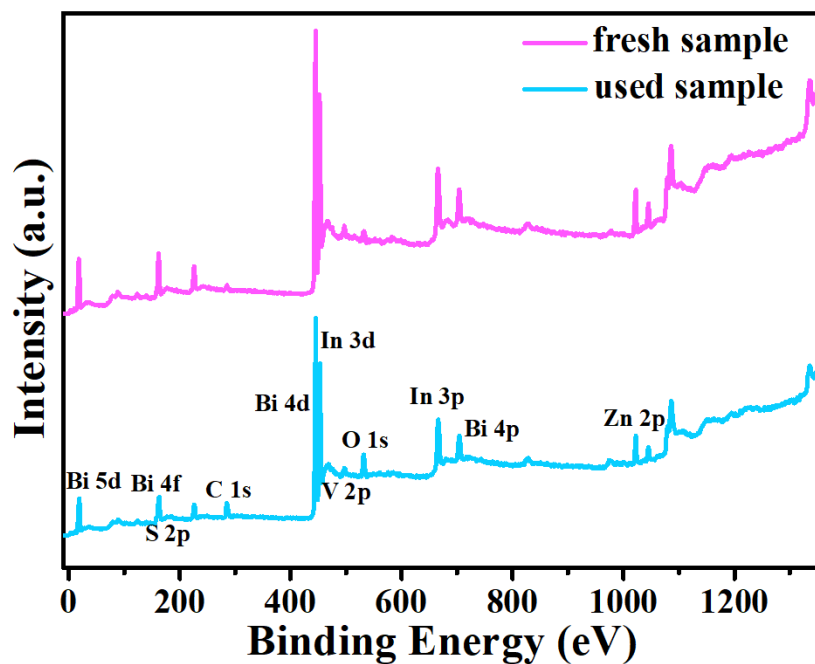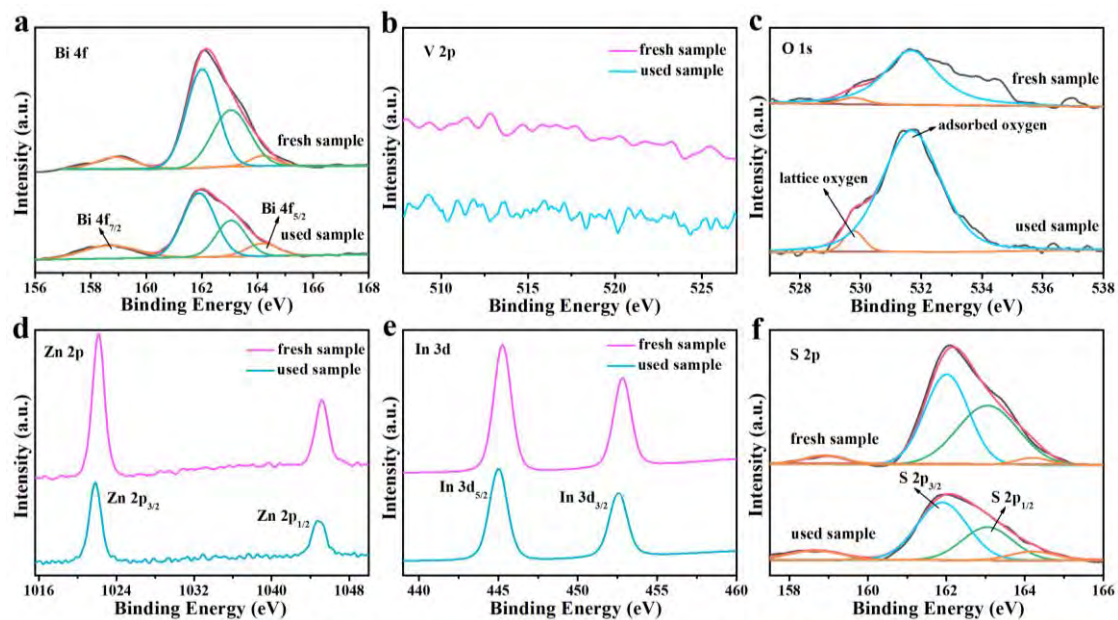

Fig. S7. TOC removal of (a) ZIS, BVO and ZIS/BVO-0.10, (b) Cycling experiments,

(c) XRD patterns, and (d) SEM image of ZIS/BVO-0.10 after cycling.

Fig. S8. XPS survey spectra of the fresh and the used ZIS/BVO-0.10.

Fig. S9. The high resolution XPS spectra of (a) Bi 4*f*, (b) V 2*p*, (c) O 1*s*, (d) Zn 2*p*, (d) In 3*d* and (f) S 2*p*.